Revision 2

A siltstone reaction front related to CO_2 and sulfur bearing fluids: Integrating quantitative elemental mapping with reactive transport modeling

Alexandra Maskell[1], Peter M. Scott[1], Iris Buisman[1], Mike Bickle[1]

[1]Department of Earth Sciences, University of Cambridge, Downing Street, Cambridge CB2 3EQ, UK

Abstract

For the purpose of geological carbon storage, it is necessary to understand the long-term effects of introducing CO_2 and sulfur-species into saline aquifers. CO_2 stripped from the flue gas during the carbon capture process may contain trace SO_2 and H_2S and it may be economically beneficial to inject S-bearing CO_2 rather than costly purified CO_2. Further, reactions between the S-bearing CO_2, formation brines and formation minerals will increase pH and promote further dissolution and precipitation reactions. To investigate this we model reactions in a natural analogue where CO_2 and SO_4-H_2S bearing fluids have reacted with clay-rich siltstones. In the Mid-Jurassic Carmel formation in a cap rock to a natural CO_2-bearing reservoir at Green River, Utah, a 3.1 mm wide bleached alteration zone is observed at the uppermost contact between a primary gypsum bed and red siltstone. Gypsum at the contact is ~1 mm thick and shows elongate fibers perpendicular to the siltstone surface, suggesting fluid flow along the contact. Mineralogical concentrations, analyzed by Quantitative Evaluation of Minerals by SCANning electron microscopy (QEMSCAN), show the altered siltstone region comprises two main zones, a 0.8 mm-wide hematite-poor, dolomite-poor and illite-rich region adjacent to the gypsum bed and a 2.3 mm-wide hematite-poor, dolomite-poor, illite-poor region adjacent to the hematite alteration front. A one-component analytical solution to reactive-diffusive transport for the bleached zone

implies it took less than 20 years to form before the fluid self-sealed, and that literature hematite dissolution rates between 10^{-8} and 10^{-7} mol/m^2/s are valid for likely diffusivities. Multi-component reactive-diffusive transport equilibrium modeling for the full phase assemblage, conducted with PHREEQC, suggests dissolution of hematite and dolomite and precipitation of illite over similar short timescales. Reaction progress with CO_2-bearing, SO_4-rich and minor H_2S-bearing fluids is shown to be much faster than with CO_2-poor, SO_4-rich with minor H_2S-earing fluids. The substantial buffering capacity of mineral reactions demonstrated by the S and CO_2–related alteration of hematite-bearing siltstones at the Green River CO_2 accumulation implies that corrosion of such a cap rock are, at worst, comparable to the 10,000-year timescales needed for carbon storage.

Keywords: reactive-transport modeling, Green River CO_2 accumulation, QEMSCAN, PHREEQC

Introduction

Storing anthropogenic carbon dioxide (CO_2) in geological reservoirs is a primary option to mitigate climate change. One of the perceived risks of carbon storage is the leakage of stored carbon dioxide (CO_2) through cap rocks, faults and fractures. To quantify these risks through the life of an individual carbon storage site it is essential to understand the geochemical behavior and evolution of CO_2 in geological reservoirs over a range of time-scales. Best practice guidelines suggest leakage rates of less than 0.01% of the volume stored per year and storage times on the order of several thousand to 10,000 years are required to ensure that storage sites meet the ultimate aim of mitigating climate change (Chadwick et al. 2008).

CO_2 stripped from the flue gas during the carbon capture process is likely to contain trace (< 5 %) co-containments, i.e. SO_2, H_2S, NOx and O (Talman 2015). To purify the gas further is a costly process and hence, if CO_2 can be safely stored with these co-contaminants it will be economically beneficial. When SO_2 dissolves in groundwater it may form H_2SO_3, H_2SO_4 or H_2S depending upon redox conditions, and these compounds are stronger acids than dissolved carbonate species formed through CO_2 dissolution. The resulting decreases in pH and pe are likely to result in enhanced mineral dissolution and precipitation at the gas-groundwater interface (e.g. Knauss et al. 2005; Xu et al. 2007; Wilke et al. 2012). Only a few studies have investigated the short term impact of these coupled reactions through either batch reactor experiments (Dawson et al. 2015; Pearce et al. 2015a,b) or field experiments (Bachu et al. 2005; Kaszuba et al. 2011). Over geological time even less is known about the impact of the dissolved sulfur species and CO_2 on cap rocks and reservoir rocks. These long exposure times may lead to porosity-permeability changes from mineral precipitation and dissolution. The study of natural analogues with S and CO_2 bearing reservoir fluids are needed to constrain long term predictions of reservoir and cap rock alteration during CO_2 storage.

Natural CO_2 and CO_2- SO_4-bearing fluids have been migrating up two fault zones for > 400,000 years at Green River, Utah through sandstones, mudstones and siltstones (Burnside et al., 2013). These lithologies are typical of those proposed as geological repositories for anthropogenic CO_2. Scientific drilling adjacent to the Little Grand Wash fault in 2012 has allowed study of CO_2 transport mechanisms and long-term reactions between S-bearing CO_2-saturated brines and formation minerals in shallow aquifers (Fig. 1; Kampman et al. 2013, 2014, 2016; Busch et al. 2014). Drill-core collected in this 2012 drilling campaign exhibits bleaching in the reservoir sandstone, basal sections of the cap rocks related to these migrating fluids. The basal ~10 cm of a

siltstone bed in the middle of the Entrada Sandstone and a claystone bed at the base of the Carmel Formation are bleached where in contact with CO_2- and S-bearing reservoir fluids (see Busch et al. 2014 and Kampman et al. 2016 for further details). Small-scale bleaching is also observed within the Carmel Formation adjacent to horizontal and sub-horizontal gypsum-filled fractures. Figure 2 shows the contact between the top of a remobilized gypsum bed and the base of a red siltstone bed. This remobilized gypsum bed associated with the bleaching has a 1mm wide fibrous overgrowth perpendicular to bedding where in contact with the siltstone, suggesting fluid flow along a previously open fracture. Numerous gypsum filled fractures have been comprehensively documented and investigated in the core indicating gypsum-saturated fluids were common (Chen et al. 2016). Additionally, celestine and gypsum have been found as fracture fill at surface in the study area (Dockrill 2006). This is supported by the modern day fluids, which are mildly reducing, and CO_2-saturated at depth (< ~320 m) with minor S and CH_4 (Kampman et al. 2014).

In this paper we use mapping of quantitative elemental mineralogy by QEMSCAN techniques to calibrate reactive transport modeling. The modeling is used to determine the duration of the bleaching event and the sensitivity of the bleaching reactions to fluid composition; specifically, the impact of CO_2-bearing fluids on clay-rich siltstones.

Regional Geology

Near the town of Green River, natural CO_2-bearing fluids are hosted in a series of fault bounded Jurassic sandstone reservoirs in the footwall blocks of the southerly dipping Little Grand Wash and Salt Wash normal faults, where they intersect the apex of the Green River anticline (e.g. Heath et al. 2009; Dockrill and Shipton 2010; Kampman 2009, 2012, 2013; Shipton et al. 2004;

Wigley et al. 2012). The CO_2-bearing fluids escape to the surface through the fault damage zones of the faults as well as a number of abandoned petroleum exploration and water wells (Fig. 1) where they form a series of CO_2 springs and geysers (Heath, 2004; Kampman et al. 2009; Dockrill and Shipton 2010; Shipton et al. 2004, 2005). Ancient travertine deposits along the faults attest to CO_2 leakage for at least 400,000 years (Burnside et al. 2013). The intermittent travertine deposition is driven by the CO_2-leakage with an episodicity controlled by climate driven changes in the hydraulic behaviour of the faults (Kampman et al. 2012). Meteoric fluid flows in the sandstone reservoirs from recharge regions in the northern San Rafael Swell to discharge in the Green River, south of the Green River anticline (Hood and Patterson 1984). Fluid flow is parallel to the faults (west to east) where they are sealing, and towards the south-east where they are transmissive towards the fault tips. Artesian conditions prevail throughout the transmissive formations of the Palaeozoic stratigraphy, driving fluid migration up the normal faults to discharge at CO_2-springs at the surface. Details of the local hydrology are discussed in Kampman et al. (2009) and the regional hydrology is discussed in Hood and Patterson (1984). The regional burial diagenesis of the Jurassic strata includes development of hematite and goethite grain coatings, giving the rock its characteristic red color (Cullers 1995; Trimble and Doelling 1978). Proximal to hydrocarbon seeps and CO_2 accumulations, extensive bleaching has occurred (e.g. Beitler et al. 2003, 2005; Parry et al. 2004; Wigley et al. 2012). At Green River, Wigley et al. (2012) document bleaching at the base of the stratigraphy in Salt Wash Graben, ascertaining that the reducing fluid (i.e. CO_2-S-bearing brines) must be more dense than the formation fluid. The modern fluids in the Entrada and Navajo Sandstone are CO_2 and SO_4 -rich with a low pH of 5.1. Furthermore, Eh measurements of spring and geyser waters indicate the fluids are mildly reducing (0 to -50 mV; Kampman et al. 2014). Analyses of fluid inclusions by

Wigley et al. (2012) and exsolved gas compositions from the springs by Kampman et al. (2014) show these fluids also contain trace quantities of CH_4 (0 – 28 %), a known reducing agent. Kampman et al. (2014, 2016) inferred that reduced sulfur must be playing a role in the bleaching given the mildly reducing groundwater (0 to -50 mV which implies that the fluids with ~20 mmol/L SO_4 contain ~ 0.5 mmol/L H_2S) coupled with the evidence for precipitation of pyrite in the basal portions of the Entrada and Carmel cap rocks. CO_2 -bearing core experiments conducted by Purser et al. (2014) on red Entrada Sandstone showed H_2S is most likely the main driver for bleaching. Using 1 mg/l of thioacetamide (which breaks down on the addition to water releasing reduced sulfur) the authors were able to reduce all the Fe^{3+} in the core sample to Fe^{2+} (mobilizing 15 mg/l of iron), thus bleaching the entire sample in the 6-month experiment. Whereas, using 5% CH_4 they were only able to mobilize at best one fifth (3 mg/l) of the iron in 6 months. It is evident that the kinetics of the hematite dissolution reaction are much faster with H_2S rather than with CH_4 as the reducing agent. Given this evidence, H_2S is considered to be the primary reductant in the Green River CO_2 accumulation.

Fluid migration and subsequent alteration in the region likely occurred either: (i) pre-CO_2 accumulation during uplift associated with the formation of the Colorado Plateau after the Eocene (S-bearing CO_2-poor fluids), or (ii) synchronous with the CO_2 accumulation and possibly relating to the periodic recharging of the reservoir during the Quaternary (S-bearing CO_2-saturated fluids; Kampman et al. 2012).

Local Geology

Scientific drilling into the Green River CO_2 accumulation (see Kampman et al. 2013) intersected the Entrada Sandstone, Carmel Formation and the Navajo Sandstone. Within the Carmel Formation a red siltstone layer is bleached where it is in contact with a gypsum vein adjacent

to the top of a primary gypsum bed. The Carmel Formation is a 50 m-thick complex lithologically heterogeneous package representing units that were deposited in environments ranging from aeolian, fluvial, coastal sabkha to shallow and open marine (Blakey et al. 1983, 1988). The documented bleached contact occurs at 158.34m below surface within a package of interbedded, unfossiliferous red and grey siltstone/shale and bedded gypsum/anhydride (Fig. 2). Extensional faulting within the Carmel Formation has resulted in the re-mobilization of many of these gypsum and anhydride beds, along with the brecciation of siltstone beds and formation of gypsum-filled open fractures. It is above one of these gypsum filled open fractures adjacent to the top of a primary gypsum bed where 3.1 mm of a red siltstone bed is bleached. The bleaching is suggestive of penetration of reducing CO_2-saturated fluids by diffusion and subsequent alteration of the siltstone mineralogy.

Analytical Methods

The small-scale of this alteration front, means using standard techniques (i.e. subsampling for XRD and XRF measurements) for determining quantitative mineralogical and chemical changes is challenging. As such, in this study we take a different approach by quantifying mineralogical profiles from QEMSCAN analyses and coupling these with reactive transport modeling. QEMSCAN is a proven technique recently becoming popular with industry and research organisations including studies relating to CO_2 storage (e.g. Petrel Sub-Basin, NT, Australia; Consoli et al. 2014). Generally good agreement has been seen with XRD analyses (Wunsch et al. 2014; Farquhar et al. 2015; Pearce et al. 2016).

Mineralogical and elemental maps were made of a thin section across a gypsum-siltstone reaction front located in the drill-core at 158.34m below surface from the drill-hole CO2W55

(Fig. 2; Kampman et al. 2013). The quantitative elemental maps were obtained using a Quanta 650F, Field Emission Gun (FEG) Scanning Electron Microscope (SEM), equipped with two Bruker XFlash 6130 Energy Dispersive Spectrometers (EDS) at the Department of Earth Sciences, University of Cambridge. The fully automated system includes an automated spectrum acquisition and classification procedure. Analyses were performed by obtaining field-scans (i.e. phase maps) across the areas of interest thus providing a complete characterization of particle surfaces above a predefined electron backscatter threshold. The brightness coefficients were calibrated against quartz, gold and copper. Spectra were collected at 15 kV and 10 nA with 2000 total X-ray counts per pixel at a 1.5 micrometer spacing, and compared to a Species Identification Protocol (SIP) that discriminates minerals on the basis of their characteristic X-ray and electron backscatter intensities. Data was processed further through a FEI software package under development, NanoMin, which has a better capacity in dealing with solid solutions allowing for superior resolving power of the chemistry in each pixel. This software package was used to obtain mineralogical and elemental maps illustrating the textural and chemical relationships across the reaction front. XRD is better for clay identification, however it requires a larger amount of sample and only gives a bulk measurement. In comparison, QEMSCAN is particularly powerful for small samples. Additionally, it provides information on the relationships between morphology, texture and chemistry in a mapped area which is useful for this application.

Mineralogical Changes

The early diagenetic mineralogy of the siltstones in the Carmel Formation is dominated by illite, quartz, dolomite, ankerite, K-feldspar, albite and hematite (Table 1; Fig. 3). The contacts

between the gypsum/anhydride beds and the siltstone beds mapped in the drillcore (Kampman et al. 2014) show no evidence of alteration with the exception of one upper contact of a gypsum bed at 158.34 meters where a ~3.1 mm-thick zone of alteration occurs in the siltstone adjacent to the gypsum bed. Chen et al. (2016) measured the hydration waters of this gypsum bed at 158.48 m, the sample comprised 19.7 % H_2O. Figures 3 and 4 show the major mineralogical profiles of the alteration zone adjacent to the gypsum bed as revealed by QEMSCAN analyses. The mineralogy across the reaction front is determined by the NanoMin software using mineral compositions of:

Albite: $NaAlSi_3O_8$

Ankerite: $CaFe_{0.7}Mg_{0.3}(CO_3)_2$

Dolomite: $CaMg(CO_3)_2$

Hematite: Fe_2O_3

Illite: $K_{0.97}(H_3O)_{0.4}Al_{2.46}Fe_{0.3}Mg_{0.17}Ti_{0.03}Si_{3.07}O_{7.15}(OH)_2 \cdot (H_2O)$

Orthoclase/Microcline: $K(AlSi_3O_8)$

Quartz: SiO_2

It is evident from Figure 3 and Figure 4 that there are two dominant alteration zones: (1) a ~2 mm wide zone of Fe dissolution adjacent to the sharp bleached-red transition, and (2) a ~1 mm zone of Fe, dolomite, orthoclase/microcline and albite dissolution, and the precipitation of illite in the siltstone adjacent to the gypsum bed. The QEMSCAN analysis indicates that only minor hematite is present in the unaltered sample and instead the Fe is bound in Fe-illite and ankerite (ankerite has a similar spatial distribution to dolomite). Whether the hematite is too fine grained to resolve or Fe-illite is actually present is not known. XRD analysis of the compositionally

similar Carmel cap rocks suggests the Fe is bound in hematite (Kampman et al. 2016). For the purpose of modeling the geochemical profile it is assumed the Fe is in hematite.

A ~1 mm zone of elongate, fibrous gypsum is present at the contact between the gypsum and the siltstone with the fibers growing with the growth generally perpendicular to the contact (Fig. 5). Fibrous gypsum normally precipitates within fractures to form veins (e.g. Machel 1985; Raman and Ramdas 1954; Warren 2006) therefore the presence of these structures at the contact, implies the vein has undergone extension and thus at one point in time a fracture opened between these two sedimentary units. This extensional period causing the open fracture could either be associated with the uplift of the Colorado Plateau in the Cenozoic (Flowers 2010) or with later de-glaciation events during crustal flexing from the glacial unloading of Lake Bonneville, Cutler Dam or Little Valley (Kampman et al. 2012). The observed petrological changes in the adjacent bleached zone are consistent with a series of dissolution reactions involving CO_2, SO_2 and H_2S which result in the removal of hematite, dolomite, orthoclase and albite via stoichiometries such as,

Hematite dissolution:

$$4Fe_2O_3 + H_2S + 14CO_2 + 6H_2O \rightarrow 8Fe^{2+} + SO_4^{2-} + 14HCO_3^-$$

$$Fe_2O_3 + 2HS^- + 4CO_2 + H_2O \rightarrow Fe^{2+} + FeS_2 + 4HCO_3^-$$

Dolomite dissolution:

$$MgCa(CO_3)_2 + 2H^+ \rightarrow Mg^{2+} + Ca^{2+} + 2HCO_3^-$$

$$MgCa(CO_3)_2 + 2H_2CO_3 \rightarrow Mg^{2+} + Ca^{2+} + 4HCO_3^-$$

$$MgCa(CO_3)_2 \leftrightarrow Mg^{2+} + Ca^{2+} + 2CO_3^{2-}$$

Orthoclase/Microcline dissolution:

$$K(AlSi_3O_8) + 9H^+ \rightarrow K^+ + Al^{3+} + 3H_3SiO_4$$

Albite dissolution:

$$NaAlSi_3O_8 + 9H^+ \rightarrow Na^+ + Al^{3+} + 3H_3SiO_4$$

The released cations of Fe, Mg, K, and Al can then react form illite, i.e. by the illitization of kaolinite (i.e. Kohler et al. 2009).

An overall loss of Mg, Fe, Na and Ca at the siltstone-gypsum bed boundary suggests the reacting fluids transported these cations out of the system. The documented petrological changes are consistent with the stoichiometry of the reaction:

$$CO_2\,(g) + H_2S + albite + dolomite + orthoclase/microcline + hematite \rightarrow illite + ankerite + Mg^{2+} + Fe^{2+} + Na^{+} + Ca^{2+} + HCO_3^{-} + SO_4^{2-}$$

Reactive Transport Modeling

The redistribution of chemical components in groundwater is controlled by four principal processes: advection, mechanical dispersion, molecular diffusion and the rate of chemical reaction (e.g. Bear 1972; Bethke 2008). Siltstones in the Carmel formation have low permeabilities, $< 10^{-18}$ m^2, effective solute diffusivities, D_e, in the fluid phase on the order of 10^{-11} to 10^{-12} m^2 (Kampman et al. 2016), and a piezometric pressure gradient between 10^4 and 10^6 Pa/m (taken from the hydraulic head data of the Navajo Sandstone; Hood and Patterson, 1984; Kampman et al. 2016). These parameters imply a flow rate ($\omega_0\varphi$) of $< 6\text{x}10^{-10}$ m/s for the siltstones, and Peclet numbers ($Pe = \omega_0\varphi h/D_e$), the ratio of diffusive to advective timescales, between 10^{-7} and 10^{-1}. As $Pe << 1$ diffusive transport dominates and advection can be neglected in the transport equations.

To further understand the governing processes of a reactive system we use a simplified one component analytical solution, coupling chemical reactions and physical transport processes.

One Component Transport Model

For one-dimensional transport, perpendicular to the vein margin, the diffusion-reaction equation describing the change in solute concentration C (mol/m^3) with time t (s) and distance, x (m) can be written as:

$$\phi \frac{\partial C}{\partial t} = D_e \frac{\partial^2 C}{\partial x^2} + k_f \alpha (C_{eq} - C) \tag{1}$$

where D_e is the effective diffusion coefficient, k_f is the mineral reaction rate (m/s), α is the mineral surface area (m^2/m^3) and C_{eq} is the solute concentration at equilibrium. The variation in the mineral molar concentration in the rock, φ_s (mol/m^3) with time t, as controlled by surface dissolution, is modeled by a linear kinetics as:

$$\frac{\partial \varphi_S}{\partial t} = -k_f \alpha (C_{eq} - C) \ . \tag{2}$$

Following Kampman et al. (2016), the following transformations to dimensionless variables are made:

$$x = lx'$$
$$t = t' l^2 / D_e \tag{3}$$
$$C = C_{eq} - C'(C_{eq} - C_0)$$
$$x = lx'$$

where $'$ indicates a dimensionless variable and l is an appropriate length scale. The dimensionless equations describing the changing solute concentration for one-dimensional diffusive transport

with mineral reaction of over time, and the variation of mineral moles in dimensionless time (t') are, respectively:

$$\frac{\partial C\prime}{\partial t\prime} = \frac{\partial^2 C\prime}{\partial x\prime^2} + N_D C' \quad (4)$$

$$\frac{\partial \varphi_S'}{\partial t\prime} = -N_D C' \ . \quad (5)$$

The solutions for fluid compositions and hematite mineral modes are controlled by the dimensionless Damköhler number, N_D, the ratio between the rate of reaction and the rate of transport of the fluid. For diffusion dominated reactive transport (equation 1) the Damköhler number is defined by:

$$N_D = \frac{k_f \alpha l^2}{D_e} \quad (6)$$

For a mildly reducing S-bearing CO_2-saturated fluid similar to that of the downhole Navajo fluids (Kampman et al. 2014) hematite dissolution rates (k_R) of 10^{-8} to 10^{-7} mol/m^2/s are expected (dos Santos Afonso and Strumm 1992). Hematite appears to be finely disseminated in the siltstone, thus grain surface areas (α) are expected to be similar to the Carmel cap rock and are estimated to be ~ 10^6 m^2/m^3. The transport distance, l (m), is taken as the displacement of the reaction front, 3.1 mm. Damköhler numbers for the gypsum-siltstone alteration zone in the Carmel Formation are therefore estimated to be between 2 and 15. This implies that the timescale of the system is diffusion limited and it can be assumed that the reacting fluids will be close to equilibrium with the minerals. Taking these assumptions, we use the following analytical solutions to the mass transport equations, as presented in Lichtner (1988).

After onset of hematite dissolution, the time (τ_0) it takes for hematite at the vein contact to become exhausted is described, assuming a constant hematite surface area, by:

$$\tau_0 = \frac{\phi_S^\infty}{V_S k_f \alpha \Delta C_0} \tag{7}$$

where φ_S^∞ is the dimensionless volume of hematite initially present. For times, $t > \tau_0$, hematite is exhausted over distances $x \leq l$.

Once this hematite dissolution front has formed ($t > \tau_0$), the time it takes for the front to migrate an observed distance, l, is calculated by:

$$l + \frac{1}{2} q l^2 = \frac{1}{q\tau_0}(t - \tau_0) \tag{8}$$

Where q (m^{-1}) is the exponential constant giving the length scale over which fluid returns to equilibrium with the initial mineralogy and defined as:

$$q = \sqrt{\frac{k_f \alpha}{D_e}} \tag{9}$$

Note that the Damköhler number, N_D, = $(ql)^2$.

The volume fraction of hematite across the alteration front, i.e. the shape of the hematite concentration profile, over time, t, and at a distance, x, downstream of the reaction front is given by:

$$\varphi_S(x, l) = \varphi_S^\infty (1 - e^{-q(x-l)}) \tag{10}$$

Figure 6 shows the calculated position of the hematite reaction front at time, t, the geometry of which is described by equation (7). The profile primarily reflects hematite dissolution and diagenetic variations in primary hematite concentrations across the reaction front. The geometry of this profile, assuming a constant D_e, is solely dependent on the kinetics of hematite dissolution. Taking an average of the hematite volume in the red unaltered region, a line of best

fit across the profile is determined using the least squares method. Exponential constant, q, in equation (7) is therefore calculated to be 896 ± 150 m^{-1} (1σ), however, q could be as small as 472 m^{-1}. With a measured reaction front distance of l = 0.0031 m, an estimated effective diffusivity, $D_e = 5 \times 10^{-12}$ m^2/s, an estimated hematite surface area of 10^6 m^2/m^3 and an infiltrating fluid compositions akin to the downhole Navajo Sandstone fluid samples we can infer the Damköhler number, timescales and dissolution rates (Fig. 7). The calculated values of q imply a Damköhler number between 2.1 and 7.7, timescales of reaction between 4 and 20 years, for hematite dissolution rates between 2×10^{-8} and 8×10^{-6} $mol/m^2/s$ (grey shaded area; Fig. 7).

Numerical Reactive Transport Model

Modeling the effects of multiple minerals, components and simultaneous reactions requires the mass transport equations to be evaluated numerically. Such modeling of multiple mineral profiles (Fig. 3-4) provides multiple constraints. As calculated above, low Peclet numbers and high Damköhler numbers indicate the fluid transport is diffusion dominant and the fluids are close to equilibrium with the host minerals. As such, we assume instantaneous equilibrium and diffusion-only transport in the models below (to make modeling simpler and thus time efficient). The modeling of the alteration was conducted using PHREEQC 3.3.9 and the llnl.dat database (Parkhurst and Appelo 1999).

Key Parameters and Variables. The 3.1 mm wide gypsum-siltstone alteration zone was modeled as a 1 cm long 1D reactive-diffusive model comprising of 20 cells of 0.5 mm length. The choice of input parameters to the reactive transport model can have a significant impact on the conclusions reached. Variables, including the thermodynamic parameters of the relevant

mineral and aqueous species, and their diffusivities are assumed to be constant. These variables are taken from the thermodynamic database llnl.dat, with diffusivities taken from direct measurements of the similar Carmel cap rock. The porosities and mineral volumes are based on quantitative elemental mineralogy (QEMSCAN) maps (Table 1). Phases allowed to dissolve and precipitate in this model were hematite, dolomite, orthoclase/microcline, albite, ankerite, gypsum, illite and quartz. The phases were chosen based on the mineralogical maps across the reaction front. The thermodynamic parameters for ankerite ($Mg_{0.3}Fe_{0.7}Ca(CO_3)_2$) were taken from TOUGHREACT's thermodynamic database (Xu et al. 2011). The initial pore fluid composition of the siltstone was taken to be a fluid calculated to be in equilibrium with the unaltered siltstone mineralogy, and with pCO_2, pO_2 and salinity estimates as that for typical Jurassic marine shales (Turrero et al. 2006, Kampman et al. 2016; Table 2). The infiltrating fluid was taken to be a fluid in equilibrium with gypsum and saturated with CO_2.

Two sets of simulations were run to investigate whether the siltstone alteration zone adjacent to the gypsum vein was associated with the infiltration of: (i) a CO_2-poor SO_4–rich fluid likely relating the uplift of the Colorado Plateau after the Eocene, or; (ii) a CO_2-SO_4–saturated fluid relating to the recharge phase of the CO_2-accumulation due to fluid movements during the Quarternary, perhaps triggered by deglaciations (Kampman et al. 2012). Since the composition of the bounding fluid in the vein is unknown, the basal Navajo Sandstone downhole fluid sample (DFS004; Kampman et al. 2014) is used varying its CO_2 content from saturated (Model 1) to CO_2-poor (Model 2). The starting compositions of the bounding fluids are shown in Table 2. A third set of models (Model 3) were run to test the sensitivity of the fronts to effective diffusivity, with the CO_2-SO_4-saturated fluid as the infiltrating fluid. All infiltrating fluids were initially

equilibrated with gypsum. The models used PHREEQC assuming diffusive transport in the fluid phase and local mineral-fluid equilibrium and were run for 100 years with a time step of 7 days.

Uncertainties. A Monte-Carlo approach is used to assess uncertainties contributions from infiltrating fluid compositions and effective diffusivity. Additional uncertainties in the numerical modeling are associated with thermodynamic databases and the assumption of instantaneous fluid-rock equilibrium.

Model 1 and Model 2 were run for 1000 Monte-Carlo iterations with the components Al, Ca, Mg, K, Na, Si, SO_4^{2-}, H_2S, pe and dissolved inorganic carbon (DIC; Table 2) in the bounding fluid being randomly varied in each iteration by ±10% (normal random distribution) relative to their listed concentrations. Cl concentrations were adjusted to maintain charge balance as Cl concentration are independent of reactions. In Model 3, 10 iterations were run where effective diffusivity was varied and bounding fluid composition kept constant for the CO_2-saturated case only. Of the 1000 simulations in Models 1 and 2, 13 of the CO_2-saturated simulations and 3 of the 1000 CO_2-poor simulations fail to converge within the 100 iterations specified by default in PHREEQC's numerical equation solver. None of the 10 effective diffusivity simulations in Model 3 failed to converge. Changes in DIC, pe, H_2S and SO_4^{2-} have the largest impact on final mineral modes.

Results

The results of the reactive transport models are shown after 6 years of diffusion in Figure 8 and Figure 9. A 6 year time step is shown because it is the best fit to observations, this is discussed further below. The hematite and dolomite reaction fronts progress quicker with the CO_2 -SO_4^{2-}-saturated infiltrating fluid. Critically the CO_2-poor infiltrating fluid did not precipitate illite in

any of the model runs. The peak in illite concentration in the core sample fracture is observed by quantitative elemental mineralogy (Fig. 4) adjacent to the gypsum bed, and is reproduced best by the CO_2 -SO_4^{2-}-saturated model, suggesting the alteration is associated with the CO_2-accumulation. Additionally, the velocity of the hematite reaction front is directly related to the concentration of H_2S and the H_2S/SO_4^{2-} ratio in the infiltrating fluid. Faster front velocities are associated with a greater H_2S concentration in the infiltrating fluid. In several simulations in both Model 1 and Model 2 dolomite precipitates at $x = 0$, where the bounding fluid is dolomite saturated. However, there is no mineralogical evidence for dolomite precipitation at the margin of the vein or in the basal contacts of siltstones with the Navajo sandstone in the Green River CO_2 accumulation, which may be a consequence of kinetic limitations on dolomite precipitation rates. In the absence of diffusivity measurements, effective diffusivity for the siltstone is approximated by the stratigraphically lower Carmel claystone cap rock (5×10^{-12} m^2; Kampman et al. 2016). In general, siltstones show slightly larger diffusivity than claystone. As shown in Figure 9, increasing effective diffusivity to 1×10^{-11} m^2 increases the velocity of the reaction front with the doubling of diffusivity causing the expected $\sqrt{2}$ increase for diffusive transport. The uncertainty in diffusivity is a fundamental limitation on the inference of timescales.

Comparison between Analytical and Numerical Models, and Petrological Observations. Both the analytical hematite model and the multi-component PHREEQC reactive-diffusion model using the gypsum-saturated basal down-hole fluid sample, give similar reproductions of the observed petrological trends. The solutions of the analytical model imply that the hematite reaction front took between 4 and 20 years to propagate 3.1 mm given hematite reaction rates of the order of 2×10^{-8} and 8×10^{-6} mol/m^2/s. A comparison at a 6 year time step between the CO_2-

SO_4 -saturated model numerical model and petrological observations from QEMSCAN is shown in Figure 10. The model predicts dissolution of albite, hematite and dolomite upstream of the hematite reaction front, and growth of secondary illite adjacent to the gypsum bed. The latter is not predicted by models of CO_2-poor fluids. Discrepancies between the observed mineral profiles and the CO_2-saturated simulations can be explained by the simplifying assumptions inherent in the models, that is, homogenous effective diffusivity, homogenous initial mineral modes and local fluid-solid equilibrium between fluids and mineral phases. A least squares fit between the Monte Carlo simulations and the observed mineralogical profile gave a best fit at $6.1^{+2.0}_{-1.0}$ years (uncertainties reflecting uncertainties in fluid compositions) since the start of CO_2-SO_4-saturated brine injection (Figure 10). This is comparable to the time estimates of the analytical model for hematite dissolution. The estimate of diffusivity is the main source of uncertainty where time scales as the inverse of diffusivity. If the fracture was actively precipitating gypsum during this time it would give an average linear extension rate of gypsum ~ 0.17 mm/year. It is very unlikely precipitation occurred at a uniform rate though time, but this rate is comparable to the rapid carbonate extension rates reported in Frery et al. (2016) for veins in travertine mounds near Green River.

Discussion

This study has shown that QEMSCAN is an extremely useful technique for investigating and quantifying the mineralogy of small scale alteration fronts. These observed mineralogical profiles (as measured by QEMSCAN) in the siltstone adjacent to the gypsum bed can be explained in terms of the interplay of mineral reactions and diffusive transport of a reactive infiltrating fluid. The alteration comprises two main zones a ~ 0.8 mm-wide hematite-poor,

dolomite-poor and illite-rich region adjacent to a gypsum bed and a ~ 2.3 mm-wide hematite-poor, dolomite-poor, illite-poor region adjacent to the hematite alteration front. There is an apparent decrease in porosity adjacent to the gypsum-siltstone contact (0 mm) from 0 to 0.8 mm and increase in porosity from 0.8 to 1.7 mm compared to the unaltered red siltstone region. Overall there is no net change in porosity between the altered region and the unaltered region, however, without BET measurements it is difficult to draw confident conclusions about the effect the CO_2-S bearing fluids had on the sealing capabilities of the siltstone. The integration of quantitative elemental mineralogical maps and reactive transport modeling has given consistent results with an estimated reaction time of 4 to 20 years from analytical modeling and ~ 6 years from numerical modeling required to produce the observed mineralogical alteration profiles given the assumed diffusivity of $5x10^{-12}$ $m^2.s^{-1}$. It is also clear from the modeling that the illite reaction profile is dependent on the dissolution of orthoclase/microcline and dolomite, however, it could also be due to primary variations in clay content. Unlike the Carmel cap rock reaction profile discussed in Kampman et al. (2016), the Entrada cap rock (Busch et al. 2014), and the Entrada Sandstone reaction front around Salt Wash Graben (Wigley et al. 2012, 2013), there are no concentration peaks in metal sulfides or metal oxides upstream of the hematite reaction front. This is likely due to the lower concentration of Fe in the unaltered siltstone, with ~4 wt. % and 2 wt. % hematite in the unaltered Carmel and Entrada cap rocks, respectively, compared to a hematite concentration of 0.4 wt. % in this study (Busch et al. 2014; Kampman et al. 2016).

At long time-scales, assuming self-sealing does not occur, the numerical model predicts it would take 5,000 year for the bleaching front to propagate ~10 cm. This is two orders of magnitude faster than > 100,000 years predicted for the Carmel and Entrada cap rocks (Busch et al. 2014;

Kampman et al. 2016). This discrepancy is due to a greater concentration of hematite in the unaltered Entrada and Carmel cap rocks. It is clear that the greater the hematite concentration, the stronger the buffering capacity of the CO_2-S fluid-rock reactions will be.

Other studies of CO_2 altered siltstone and claystone caprocks have found similar mineralogical trends to those seen in this study (i.e. Busch et al. 2014; Kampman et al. 2016). Gypsum precipitation has been documented in the Carmel caprock where gypsum fills bedding parallel fractures (Kampman et al. 2016). Kohler et al. (2009) found that at low temperature and pressures in clayey caprocks CO_2 alteration resulted in the formation of Fe^{2+}-and K^{+}-enriched illites. Overall this study agrees with those of Busch et al. 2014 and Kampman et al. 2016 who found that CO_2-S-related fluid-rock reactions have the capability to buffer the corrosive nature of the fluids, allowing cap rocks to maintain their sealing capabilities.

Implications

The results are important for geological carbon storage as they show that the addition of sulfur to CO_2 producing potentially corrosive fluids will not degrade the sealing capabilities of hematite-bearing mud- and siltstone-rich cap rocks in carbon storage sites over the lifetime of the storage projects. Further the timescales calculated from the modeling show that, even adjacent to an active fault zone, the fluid-filled cracks are sealed within a few years further impeding migration of CO_2-charged fluids. This coupling of high spatial resolution quantitative elemental and phase mapping by QEMSCAN with thermodynamic modeling should have a wider application to the study small scale alteration fronts in a number of different geological settings, particularly in stockwork veining and associated alteration in economic mineral deposits. This is because

standard methods which require larger sample volumes, miss small scale variability and only give phase information or bulk compositions.

Acknowledgments

We thank Shell Global Solutions for giving us access to the samples and FEI for allowing us access to the proprietary software NanoMin. Funding for Carbon Storage research at the University of Cambridge was provided by the Natural Environment Research Council (NERC) to the CRIUS consortium (NE/F004699/1), Shell Global Solutions International, and the UK Department of Energy and Climate Change (DECC) through a CCS Innovation grant. A.M. was supported by an EPSRC doctoral training grant.

References

Bachu, S., Haug, K., Michael, K., Buschkuehle, B., and Adams, J. (2005). Deep injection of acid gas in Western Canada. Developments in Water Science, 52, 623–635.

Bear, J. (1972), Dynamics of Fluids in Porous Media, Dover Publications.

Beitler, B., Chan, M.A., and Parry, W.T. (2003). Bleaching of Jurassic Navajo sandstone on Colorado Plateau Laramide highs: Evidence of exhumed hydrocarbon supergiants?. Geology, 31(12), 1041-1044.

Beitler, B., Parry, W.T., and Chan, M.A. (2005). Fingerprints of fluid flow: chemical diagenetic history of the Jurassic Navajo Sandstone, southern Utah, USA. Journal of Sedimentary Research, 75(4), 547-561.

Bethke, C. (2008), Reactive Transport. In: Geochemical and Biochemical Reaction Modelling, Cambridge University Press.

Blakey, R.C., Peterson, F., Caputo, M.V., Geesaman, R.C, and Voorhees, B.J. (1983), Paleogeography of Middle Jurassic continental, shoreline, and shallow marine sedimentation, southern Utah. In: Rocky Mountain Section (SEPM).

Blakey, R.C., Peterson, F., and Kocurek, G. (1988), 'Synthesis of late Paleozoic and Mesozoic eolian deposits of the Western Interior of the United States', Sedimentary Geology 56(1), 3-125.

Burnside, N.M., Shipton, Z.K., Dockrill, B., and Ellam, R.M. (2013). Man-made versus natural CO_2 leakage: A 400 k.y. history of an analogue for engineered geological storage of CO_2. Geology, 41, 471-474.

Busch, A., Kampman, N., Hangx, S.J., Snippe, J., Bickle, M., Bertier, P., Chapman, H., Spiers, C.J., Pijnenburg, R., Samuelson, J., and Evans, J.P. (2014). The Green River natural analogue as a field laboratory to study the long-term fate of CO_2 in the subsurface. Energy procedia, 63, 2821-2830.

Chadwick, R.A., Arts, R., Bernstone, C., May, F., Thibeau, S., and Zweigel, P. (2008). Best practice for the storage of CO_2 in saline aquifers. British Geological Survey Occasional Publication No. 14. Keyworth, UK.

Chen, F., Turchyn, A.V., Kampman, N., Hodell, D., Gázquez, F., Maskell, A., and Bickle, M. (2016). Isotopic analysis of sulfur cycling and gypsum vein formation in a natural CO_2 reservoir. Chemical Geology, 436, 72-83.

Consoli, C.P., Higgins, K., Jorgensen, D., Khider, K., Lescinsky, D.T., Morris, R., and Nguyen, V. (2013). Regional assessment of the CO_2 storage potential of the Mesozoic succession in the Petrel Sub-basin, Northern Territory, Australia: summary report. Record 2014/11. Geoscience Australia, Canberra.Cullers, R.L. (1995). The controls on the major-and

trace-element evolution of shales, siltstones and sandstones of Ordovician to Tertiary age in the Wet Mountains region, Colorado, USA. Chemical Geology, 123(1), 107-131.

Dawson, G., Pearce, J., Biddle, D., and Golding, S. (2015). Experimental mineral dissolution in Berea Sandstone reacted with CO_2 or SO_2-CO_2 in NaCl brine under CO_2 sequestration conditions. Chemical Geology, 399, 87–97.

Dockrill, B. (2006). Understanding leakage from a fault-sealed CO_2 reservoir in east-central Utah: A natural analogue applicable to CO_2 storage. PhD Thesis. Trinity College Dublin.Dockrill, B., and Shipton, Z.K. (2010). Structural controls on leakage from a natural CO_2 geologic storage site: Central Utah, U.S.A. Journal of Structural Geology, 32(11), 1768–1782.

Dos Santos Afonso, M., and Stumm, W. (1992). Reductive dissolution of iron (iii)(hydr)oxides by hydrogen sulfide. Langmuir, 8(6), 1671–1675.

Farquhar, S.M., Pearce, J.K., Dawson, G.K.W., Golab, A., Sommacal, S., Kirste, D., Biddle, D., and Golding, S.D., (2015). A fresh approach to investigating CO_2 storage: Experimental CO_2-water rock interactions in a freshwater reservoir system. Chemical Geology, 399, 98-122.

Flowers, R.M. (2010). The enigmatic rise of the Colorado Plateau. Geology, 38(7), 671–672.

Frery, E., Gratier, J.P., Ellouz-Zimmerman, N., Deschamps, P., Blamart, D., Hamelin, B., and Swennen, R. (2016). Geochemical transect through a travertine mount: A detailed record of CO_2-enriched fluid leakage from Late Pleistocene to present-day–Little Grand Wash fault (Utah, USA). Quaternary International.

Heath, J.E. (2004). Hydrogeochemical characterization of leaking carbon dioxide-charged fault zones in east-central Utah, M.S. thesis, 175 pp., Utah State Univ., Logan, Utah.

Heath, J., Lachmar, T., Evans, J., Kolesar, P., and Williams, A. (2009). Hydrogeochemical characterization of leaking, carbon dioxide-charged fault zones in east-central Utah, with implications for geologic carbon storage. In: Mcpherson, B. and Sundquist, E. eds. Carbon Sequestration and Its Role in the Global Carbon Cycle. American Geophysical Union, 147–158.

Hood, J.W., and Patterson, D.J. (1984). Bedrock aquifers in the northern San Rafael Swell area, Utah, with special emphasis on the Navajo Sandstone. State of Utah Department of Natural Resources. Technical Publication, 78, 1-128.

Kampman, N., Bickle, M.J., Becker, J., Assayag, N., and Chapman, H.J. (2009). Feldspar dissolution kinetics and Gibbs free energy dependence in a CO_2–enriched groundwater system, Green River, Utah. Earth and Planetary Science Letters, 284, 473–488.

Kampman, N., Burnside, N.M., Shipton, Z.K., Chapman, H.J., Nicholl, J.A., Ellam, R.M., and Bickle, M.J. (2012). Pulses of carbon dioxide emissions from intracrustal faults following climatic warming. Nature Geoscience, 5, 352–358.

Kampman, N., Maskell, A., Bickle, M., Evans, J., Schaller, M., Purser, G., Zhou, Z., Gattacceca, J., Peitre, E., Rochelle, C., Ballentine, C., and Busch, A. (2013). Scientific drilling and downhole fluid sampling of a natural CO_2 reservoir, Green River, Utah. Scientific Drilling, 16, 33–43.

Kampman, N., Bickle, M., Maskell, A., Chapman, H., Evans, J., Purser, G., Zhou, Z., Schaller, M., Gattacceca, J.C., Bertier, P., and Chen, F. (2014). Drilling and sampling a natural CO_2 reservoir: Implications for fluid flow and CO_2–fluid–rock reactions during CO_2 migration through the overburden. Chemical Geology, 369, 51–82.

Kampman, N., Bertier, P., Busch, A., Snippe, J., Hangx, S. J., Pipich, V., Di, Z., Rother, G., Harrington, J.F., Kemp, S.J., Evans, J., Maskell, A., Chapman, H., and Bickle, M.J. (2016). Observational evidence confirms modelling of the long-term integrity of CO_2-reservoir caprocks. Nature Communications, 7:12268.

Kaszuba, J.P., Navarre-Sitchler, A., Thyne, G., Chopping, C., and Meuzelaar, T. (2011). Supercritical carbon dioxide and sulfur in the Madison Limestone: A natural analog in southwest Wyoming for geologic carbon-sulfur co-sequestration. Earth and Planetary Science Letters, 309, 131-140.

Knauss, K.G., Johnson, J.W., and Steefel, C.I. (2005). Evaluation of the impact of CO_2, co-contaminant gas, aqueous fluid and reservoir rock interactions on the geologic sequestration of CO_2. Chemical Geology, 217, 339–350.

Kohler, E., Parra, T., and Vidal, O. (2009). Clayey cap-rock behavior in H_2O-CO_2 media at low pressure and temperature conditions: an experimental approach. Clays and Clay Minerals, 57(5), 616-637.

Lichtner, P.C. (1988). The quasi-stationary state approximation to coupled mass transport and fluid-rock interaction in a porous medium. Geochimica et Cosmochimica Acta, 52(1), 43–165.

Machel, H.-G. (1985). Fibrous gypsum and fibrous anhydrite in veins. Sedimentology, 32(3), 443–454.

Parkhurst, D.L., and Appelo, C.A.J. (1999). User's guide to PHREEQC (version 2) – A computer program for speciation, batch reaction, one dimensional transport, and inverse geochemical calculations. U.S. Geological Survey Water-Resources Investigations Report, 99(4259).

Parry, W.T., Chan, M.A., and Beitler, B. (2004). Chemical bleaching indicates episodes of fluid flow in deformation bands in sandstone. AAPG bulletin, 88(2), 175-191.

Pearce, J.K., Kirste, D.M., Dawson, G.K., Farquhar, S.M., Biddle, D., Golding, S.D., and Rudolph, V. (2015a). SO_2 impurity impacts on experimental and simulated CO_2-water-reservoir rock reactions at carbon storage conditions. Chemical Geology, 399, 65–86.

Pearce, J.K., Law, A.C.K., Dawson, G.K.W., and Golding, S.D. (2015b). SO_2-CO_2 and pure CO_2 reactivity of ferroan carbonates at carbon storage conditions. Chemical Geology, 10.1016/j.chemgeo.2015.07.001.

Pearce, J.K., Golab, A., Dawson, G.K., Knuefing, L., Goodwin, C., and Golding, S.D., (2016). Mineralogical controls on porosity and water chemistry during O_2-SO_2-CO_2 reaction of CO_2 storage reservoir and cap-rock core. Applied Geochemistry, 75, 152-168.

Purser, G., Rochelle, C.A., Rushton, J., Pearce, J.M., and Wagner, D. (2014). An experimental and analogue study of iron release from red sandstones. Energy Procedia, 63, 3268-3274.

Raman, C., and Ramdas, A. (1954). On the polycrystalline forms of gypsum and their optical behaviour. In: Proceedings of the Indian Academy of Sciences-Section A, v39, 153–161. Springer.

Shipton, Z.K., Evans, J.P., Dockrill, B., Heath, J., Williams, A.P., Kirschner, D., and Kolesar, P.T. (2005). Natural leaking CO_2-charged systems as analogues for failed geologic storage reservoirs. In: Benson, S., Oldenburg, C., Hoversten, M., and Imbus, S., eds. Carbon Dioxide Capture for Storage in Deep Geological Formations- Results from the CO_2 Capture Project, 699–712. Elsevier B.V.

Shipton, Z.K., Evans, J.P., Kirschner, D., Kolesar, P.T., Williams, A.P., and Heath, J. (2004). Analysis of CO_2 leakage through low-permeability faults from natural reservoirs in the

Colorado Plateau, east-central Utah. Geological Society, London, Special Publications, 233(1), 43–58.

Trimble L., and Doelling, H.H. (1978). Geology and uranium-vanadium deposits of the San Rafael River mining area, Emery County, Utah. Utah Geological and Mineral Survey Bulletin, 113, 122 p.

Turrero, M.J., Fernández, A.M., Peña, J., Sánchez, M.D., Wersin, P., Bossart, P., Sánchez, M., Melón, A., Garralón, A., Yllera, A., and Hernán, P. (2006) Pore water chemistry of a Paleogene continental mudrock in Spain and a Jurassic marine mudrock in Switzerland: Sampling methods and geochemical interpretation. Journal of Iberian Geology, 32, 233-258.

Warren, J.K. (2006). Evaporites: sediments, resources and hydrocarbons. Springer Science & Business Media.Wigley, M., Kampman, N., Dubacq, B., and Bickle, M. (2012). Fluid-mineral reactions and trace metal mobilization in an exhumed natural CO_2 reservoir, Green River, Utah. Geology, 40(6), 555–558.

Wigley, M., Kampman, N., Chapman, H., Dubacq, B., and Bickle, M. (2013). In situ redeposition of trace metals mobilized by CO_2-charged brines. Geochemistry, Geophysics, Geosystems, 14(5), 1321–1332.

Wilke, F.D.H., Vásquez, M., Wiersberg, T., Naumann, R., and Erzinger, J. (2012). On the interaction of pure and impure supercritical CO2 with rock forming minerals in saline aquifers: An experimental geochemical approach. Applied Geochemistry, 27(8), 1615-1622.

Wunsch, A., Navarre-Sitchler, A.K., Moore, J., and McCray, J.E. (2014). Metal release from limestones at high partial-pressures of CO_2. Chemical Geology, 363, 40-55.

Xu, T., Apps, J.A., Pruess, K., and Yamamoto, H. (2007). Numerical modeling of injection and mineral trapping of CO_2 with H_2S and SO_2 in a sandstone formation. Chemical Geology, 242(3), 319–346.

Xu, T., Spycher, N., Sonnenthal, E., Zhang, G., Zheng, L., and Pruess, K. (2011). TOUGHREACT Version 2.0: A simulator for subsurface reactive transport under non-isothermal multiphase flow conditions. Computers & Geosciences, 37(6), 763–774.

List of figure captions

Figure 1. Geological map of the Green River anticline showing locations of the Little Grand Wash and Salt Wash Graben normal fault systems, CO_2-springs and location of drill-hole CO2W55. Structure contours are for the top surface of the Navajo Sandstone, the main CO_2 bearing reservoir (modified after Kampman et al. 2013).

Figure 2. Sedimentary log, core photos and plane polarized light (PPL) images of the bleached alteration zone at the upper contact of the gypsum bed. Images show the bleached siltstone reaction zone at the upper contact of a gypsum bed.

Figure 3. Images of the alteration zone that occurs between an upper contact of a gypsum bed and a siltstone bed: a) Plane polarized light (PPL) photomicrograph of the region that was analyzed with QEMSCAN, and; b) Quantitative elemental mineralogy over the bleached/unbleached contact in the siltstone.

Figure 4. Images collected from QEMSCAN analyses of the alteration zone, presented are the Backscatter Electron (BSE) map, and quantitative elemental mineralogy maps; illite, kaolinite, dolomite, albite, orthoclase/microcline and hematite.

Figure 5. PPL photomicrographs of fibrous gypsum adjacent to the altered siltstone. The occurrence of fibrous gypsum at the contact implies that at one point in time there was an open fracture between these two sedimentary units allowing the flow of reactive fluids.

Figure 6. Volume fraction of hematite across the gypsum-siltstone reaction front. Squares represent the observed lithological changes as determined by quantitative mapping. The solid curve is least-squares best fit of the hematite profile to equation (7) with the shaded area representing 1σ standard deviation. The initial hematite volume, φ_S^{∞}, is the average volume over the red siltstone region. Dashed line shows profile for the minimum limit for q values of 427 m^{-1}.

Figure 7. Plot showing the solution to the analytical one-component reactive transport equations. The duration it takes for the hematite reaction front to migrate 3.1 mm calculated from equation (5) given the time for the reaction front to develop (τ_0; equation (4)). The shaded area represents the solutions for $427 < q < 896$ m^{-1}, implying time-scales of reaction between 4 and 20 years and hematite dissolution rates between 1 x 10^{-9} and 5 x 10^{-8} mol/m^2/s. Solid black line give the median solution (D_e = 5 x 10^{-12} m^2, ΔC_0 = 3.84 mol/m^3, while dashed lines show extreme solutions. Minimum estimates of D_e and ΔC_0 give maximum calculated reactions times (D_e = 1 x 10^{-12} m^2, ΔC_0 = 3.34 mol/m^3), and maximum estimates of D_e and ΔC_0 give minimum calculated reactions times (D_e = 1 x 10^{-11} m^2, ΔC_0 = 4.34 mol/m^3).

Figure 8. Diffusion-reaction modeling of gypsum-siltstone alteration zone in PHREEQC at 6 years since start of injection; with: a) CO_2-SO_4-saturated infiltrating fluid (Model 1), and; b) CO_2–poor SO_4-saturated infiltrating fluid (Model 2). 1000 iterations of each model were run (grey lines) with the infiltrating fluid compositions randomly varied ± 10 % from the compositions presented in Table 2. The black lines are the mean of all these models. The precipitation of illite in the CO_2-saturated model matches the observed mineralogical profiles the best, suggesting the fluids responsible for the alteration were CO_2-saturated.

Figure 9. Diffusion-reaction modeling of gypsum-siltstone alteration zone in PHREEQC at with a CO_2-SO_4-saturated infiltrating fluid (see Table 2 for composition). 1D models were run exactly like the models presented in Figure 8, except the effective diffusivity (D_e) was varied instead of fluid composition. Three models are plotted, with D_e of 1 x 10^{-12} m^2, 5 x 10^{-12} m^2 and 1 x 10^{-11} m^2, respectively. The plot shows the effect diffusivity has on the propagation speed of the reaction fronts.

Figure 10. Comparison between CO_2-SO_4-saturated PHREEQC model at 6 years with an effective diffusivity (D_e) of 5 x 10^{-12} m^2 and observed mineralogical profiles: a) hematite profile; b) dolomite profile, and; c) illite profile. Squares represent the average concentration over a 0.31 mm block across the alteration zone, these 26 points were determined from the QEMSCAN mineralogical maps. Model shown was the best fit to the observations of all simulation based on least squares. The modeling predicts the trends of the dissolution of hematite and dolomite

upstream of the hematite reaction front, and growth of secondary illite adjacent to the gypsum bed.

Tables

Table 1. Mineral concentrations (wt. %) determined from QEMSCAN analyses. Distances (mm) along the reaction front are measured from the gypsum-siltstone contact and the analyses are averaged over 0.3 mm.

Mineral	Unaltered Red Siltstone												
	7.65 mm	**7.35 mm**	**7.05 mm**	**6.75 mm**	**6.45 mm**	**6.15 mm**	**5.85 mm**	**5.55 mm**	**5.25 mm**	**4.95 mm**	**4.65 mm**	**4.35 mm**	**4.05 mm**
Quartz	45.96	51.71	51.65	45.62	40.38	45.47	47.19	45.07	43.09	41.81	40.23	44.84	38.77
Illite	21.53	17.22	17.73	21.93	24.03	21.34	21.00	20.26	20.26	20.14	21.86	21.35	25.14
Orthoclase	12.70	14.45	13.89	14.16	17.43	16.20	13.85	16.49	16.85	20.03	18.47	15.88	18.01
Dolomite	9.80	7.91	8.79	7.82	8.42	7.36	9.24	9.26	9.57	8.81	9.28	9.01	9.38
Kaolinite	2.88	2.97	2.52	3.10	3.24	3.70	3.21	2.56	2.97	2.68	2.55	2.44	2.13
Ankerite	3.57	2.38	2.62	3.15	2.82	2.58	2.41	2.47	3.15	2.90	3.28	2.74	2.96
Muscovite	1.85	1.47	1.42	2.37	2.34	1.96	1.71	1.74	2.23	2.08	2.40	2.07	2.03
Plagioclase	0.79	0.69	0.63	0.91	0.74	0.78	0.66	0.70	0.94	0.84	0.94	0.75	0.95
Anatase	0.11	0.32	0.12	0.14	0.07	0.12	0.16	0.16	0.51	0.22	0.14	0.22	0.16
Hematite	0.57	0.61	0.45	0.57	0.29	0.29	0.40	1.19	0.30	0.30	0.31	0.31	0.16
Apatite	0.11	0.08	0.10	0.11	0.13	0.14	0.08	0.04	0.06	0.06	0.46	0.08	0.26
Ilmenite	0.10	0.19	0.07	0.11	0.09	0.05	0.07	0.06	0.04	0.12	0.07	0.31	0.04
Zircon	0.02	0.00	0.00	0.01	0.00	0.01	0.01	0.00	0.02	0.00	0.01	0.00	0.00
Pyrite	0.01	0.00	0.00	0.00	0.01	0.00	0.00	0.00	0.01	0.01	0.00	0.00	0.00

Mineral	Unaltered Red Siltstone				Hematite-poor						Illite-rich Hem poor		
	3.75 mm	**3.45 mm**	**3.15 mm**	**2.85 mm**	**2.55 mm**	**2.25 mm**	**1.95 mm**	**1.65 mm**	**1.35 mm**	**1.05 mm**	**0.75 mm**	**0.45 mm**	**0.15 mm**
Quartz	39.93	34.35	37.14	36.43	43.58	48.05	49.16	38.01	48.16	40.92	40.84	48.36	47.57
Illite	21.52	22.75	22.21	20.89	21.15	17.91	17.03	25.85	21.10	23.04	26.03	26.88	30.81
Orthoclase	19.67	19.60	17.99	20.20	17.77	19.93	19.62	16.41	14.69	15.75	22.62	15.92	11.35
Dolomite	10.14	13.77	14.08	12.92	9.98	6.46	6.70	10.11	5.41	11.95	4.03	1.29	0.32
Kaolinite	1.88	1.71	1.68	1.76	2.23	2.69	2.97	2.76	3.39	2.56	2.74	4.13	7.71
Ankerite	2.84	3.37	3.26	3.36	2.16	1.94	1.66	2.80	2.11	2.63	0.98	0.39	0.15
Muscovite	2.01	2.31	2.13	2.44	1.88	1.83	1.91	2.53	2.28	1.71	1.34	1.35	1.14
Plagioclase	1.00	1.18	1.15	1.06	0.82	0.82	0.63	0.96	0.88	0.93	0.42	0.33	0.40
Anatase	0.32	0.36	0.15	0.43	0.23	0.15	0.15	0.25	1.50	0.30	0.60	1.02	0.38
Hematite	0.23	0.19	0.07	0.02	0.03	0.02	0.03	0.04	0.03	0.06	0.01	0.01	0.01
Apatite	0.30	0.15	0.11	0.28	0.12	0.15	0.03	0.12	0.08	0.12	0.31	0.20	0.10
Ilmenite	0.13	0.04	0.01	0.09	0.03	0.04	0.10	0.13	0.34	0.02	0.04	0.10	0.02
Zircon	0.01	0.22	0.00	0.10	0.02	0.00	0.00	0.01	0.00	0.01	0.02	0.01	0.01
Pyrite	0.01	0.00	0.00	0.00	0.00	0.01	0.01	0.00	0.00	0.00	0.01	0.02	0.02

698

Table 2. Compositions (mol/L) of initial pore water (Turrero et al. 2006), CO_2-SO_4-saturated brine (measured sample DFS004 saturated with gypsum; Kampman et al. 2014) and CO_2-poor SO_4-saturated brine used in the PHREEQC reactive transport modeling. Alk – alkalinity (mEq/L), DIC – dissolved inorganic carbon.

pH	Al^{3+}	Ca^{2+}	Mg^{2+}	K^{+}	Na^{+}	SiO_2	Cl^{-}	SO_4^{2-}	H_2S	Alk	DIC
Initial Pore Water											
7.52	0	13.6	1.63	0.43	23.9	0	30.4	23.9	0	0.76	0.8
CO_2-SO_4-Saturated Brine											
5.1	0.01	24.1	10.1	7.2	112.5	0.1	84.9	20.7	0.5	64	884
CO_2-poor SO_4-Saturated Brine											
5.1	0.01	24.1	10.1	7.2	112.5	0.1	84.9	20.7	0.5	2.5	2.5

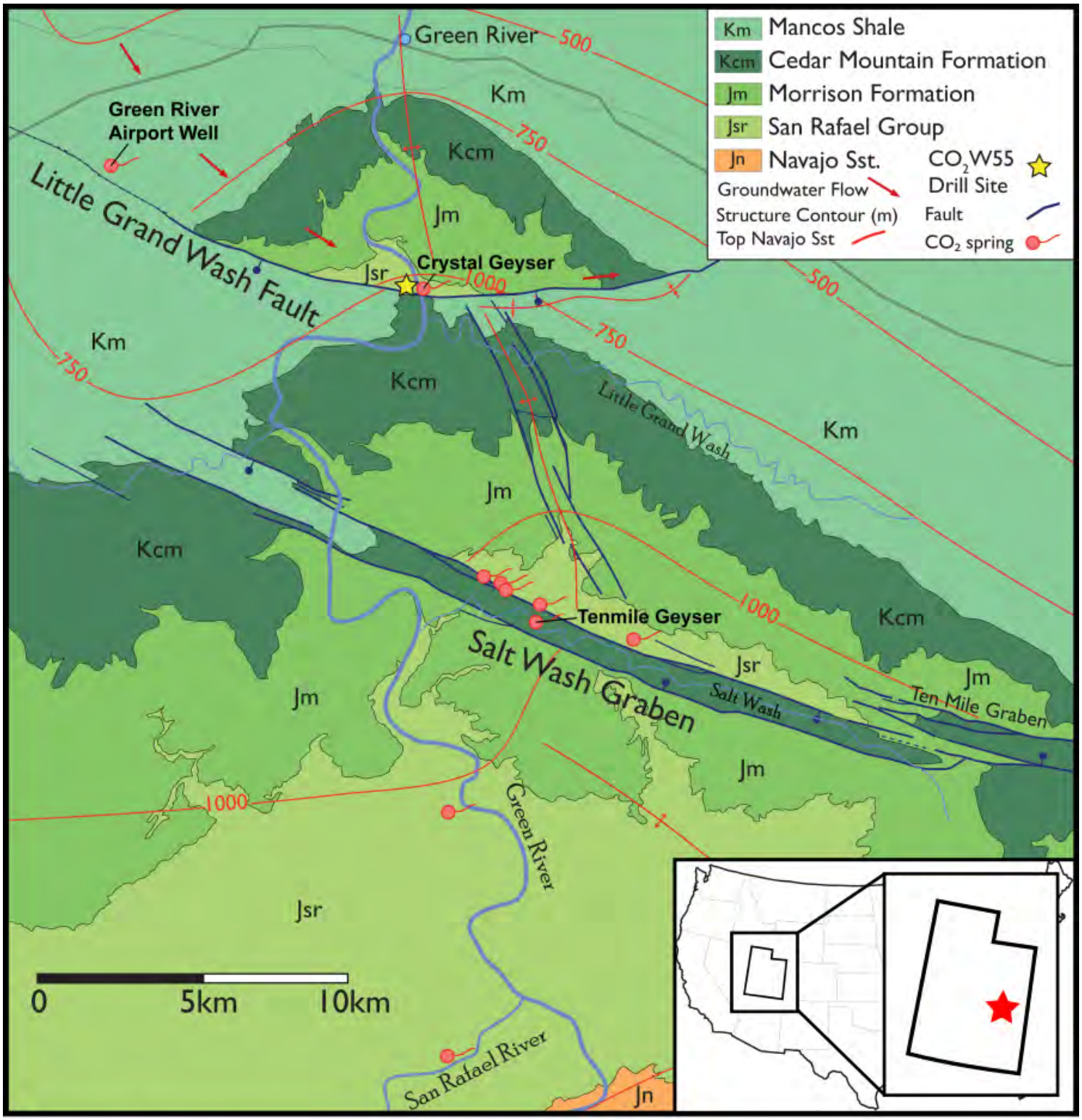
Km Mancos Shale
Kcm Cedar Mountain Formation
Jm Morrison Formation
Jsr San Rafael Group
Jn Navajo Sst.
Groundwater Flow
Structure Contour (m)
Top Navajo Sst
CO2W55 Drill Site
Fault
CO2 spring
Green River
Green River Airport Well
Little Grand Wash Fault
Crystal Geyser
Little Grand Wash
Tenmile Geyser
Salt Wash Graben
Salt Wash
Ten Mile Graben
Green River
San Rafael River
500
750
1000
0
5km
10km

Figure 1

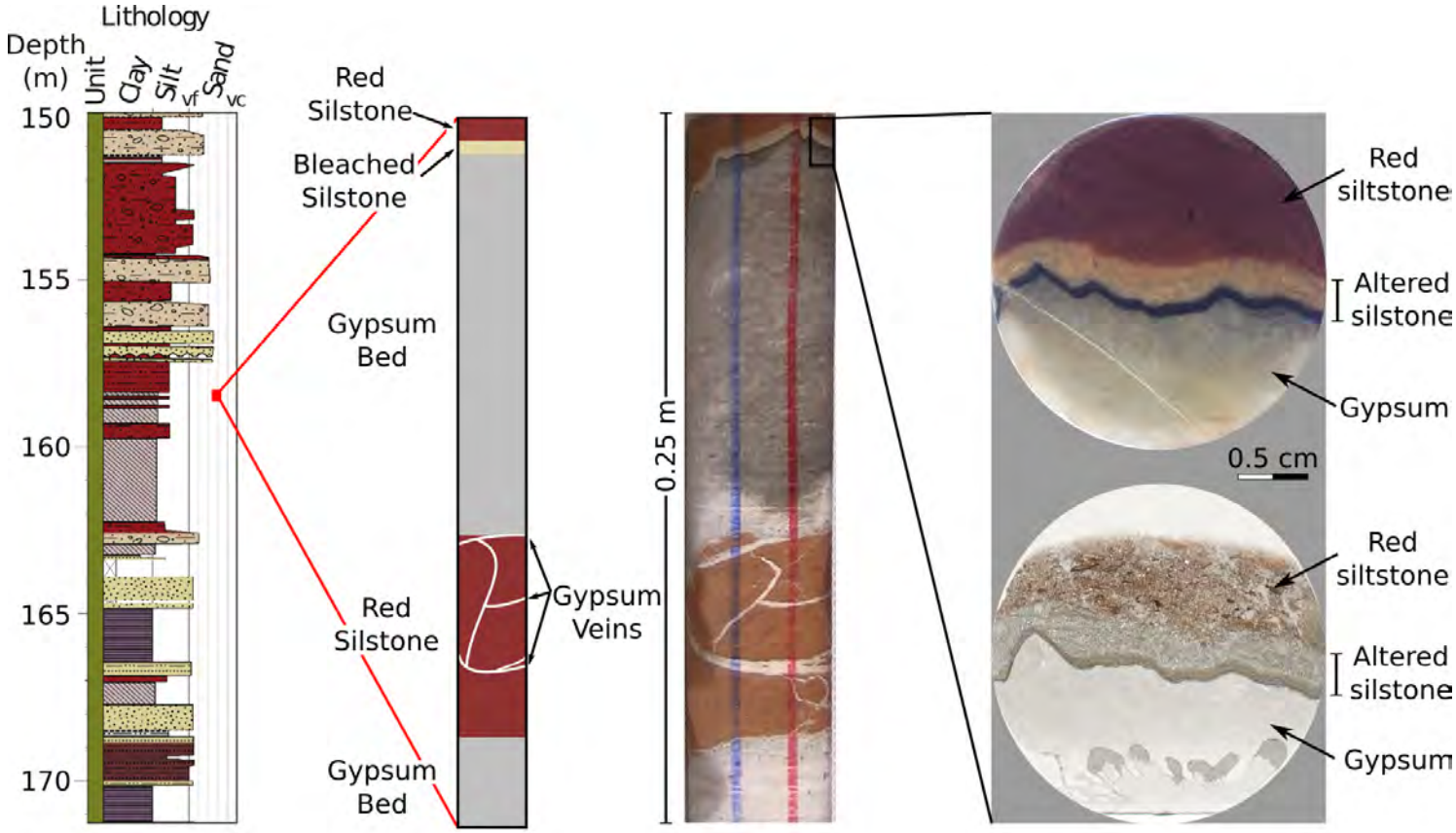
Lithology
Depth (m)
Unit
Clay
Silt
vf
Sand
vc
150
155
160
165
170
Red Silstone
Bleached Silstone
Gypsum Bed
Red Silstone
Gypsum Bed
Gypsum Veins
0.25 m
Red siltstone
Altered silstone
Gypsum
0.5 cm
Red siltstone
Altered silstone
Gypsum

Figure 2

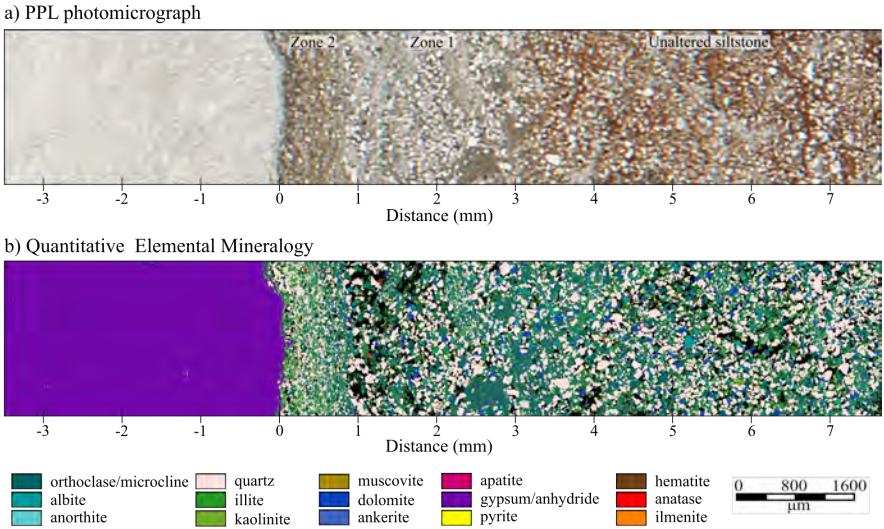
a) PPL photomicrograph
Zone 2
Zone 1
Unaltered siltstone
-3
-2
-1
0
1
2
3
4
5
6
7
Distance (mm)
b) Quantitative Elemental Mineralogy
-3
-2
-1
0
1
2
3
4
5
6
7
Distance (mm)
orthoclase/microcline
albite
anorthite
quartz
illite
kaolinite
muscovite
dolomite
ankerite
apatite
gypsum/anhydride
pyrite
hematite
anatase
ilmenite
0
800
1600
µm

Figure 3

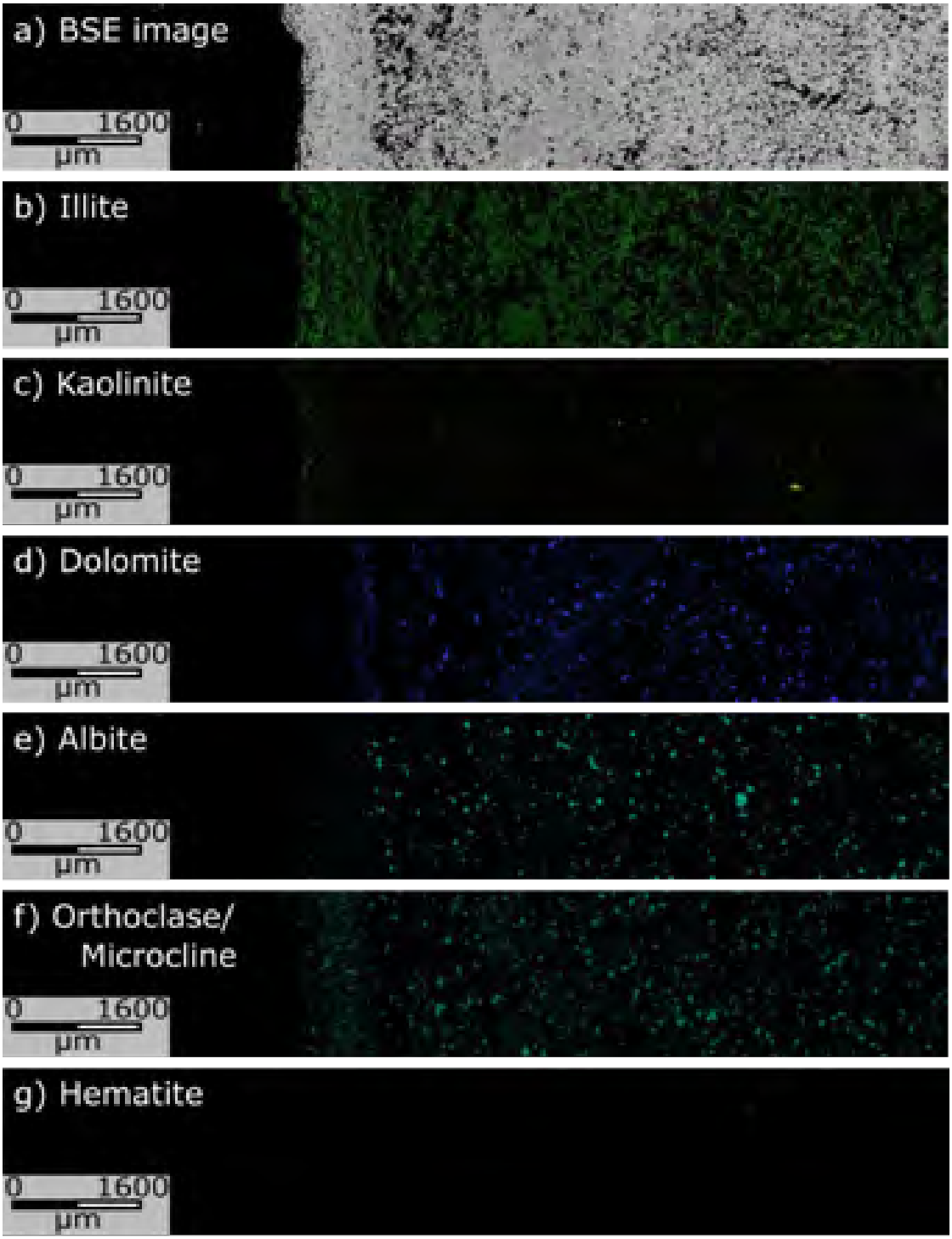
a) BSE image
0 1600
µm
b) Illite
0 1600
µm
c) Kaolinite
0 1600
µm
d) Dolomite
0 1600
µm
e) Albite
0 1600
µm
f) Orthoclase/
Microcline
0 1600
µm
g) Hematite
0 1600
µm

Figure 4

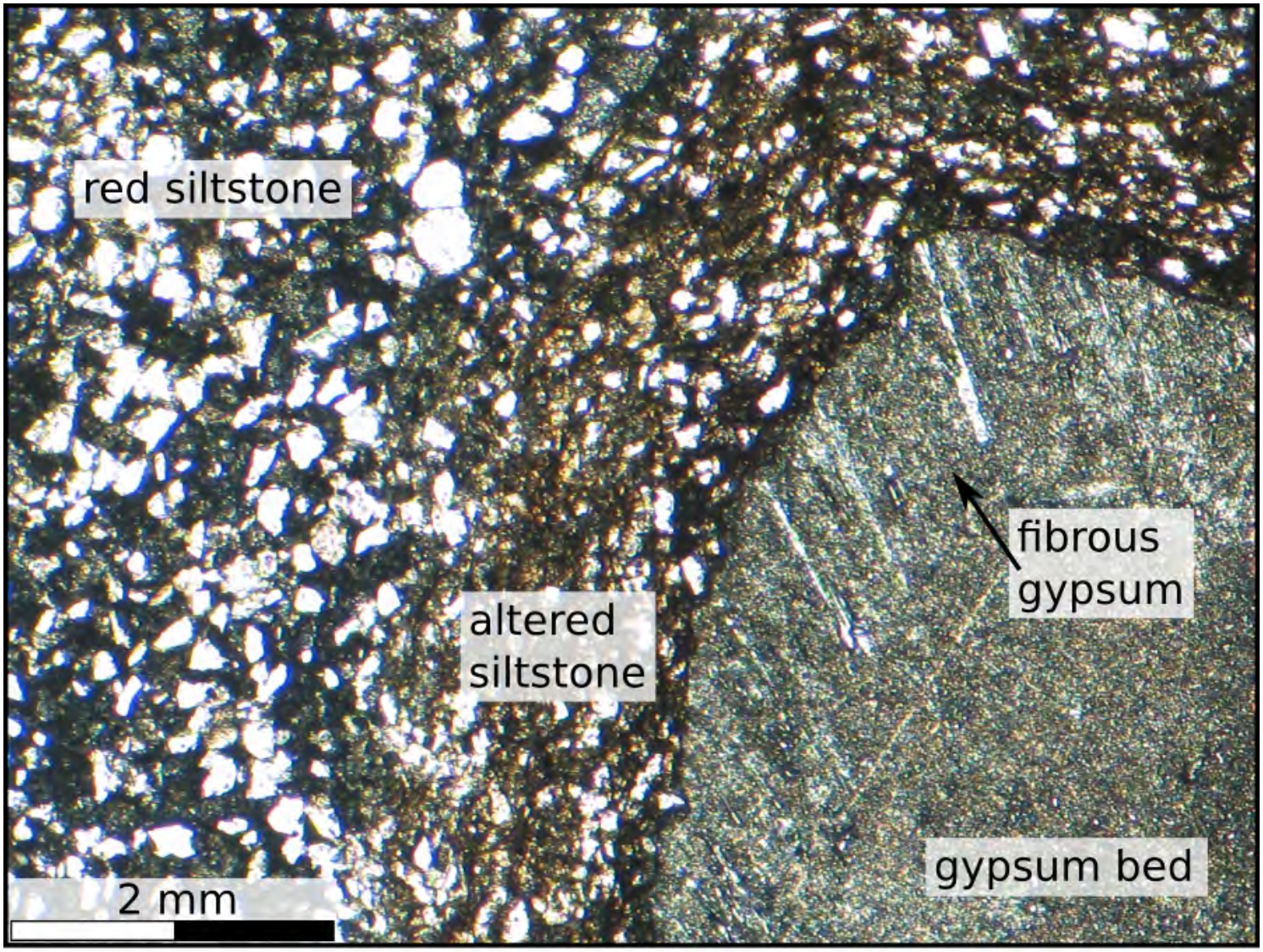
red siltstone
altered
siltstone
fibrous
gypsum
gypsum bed
2 mm

Figure 5

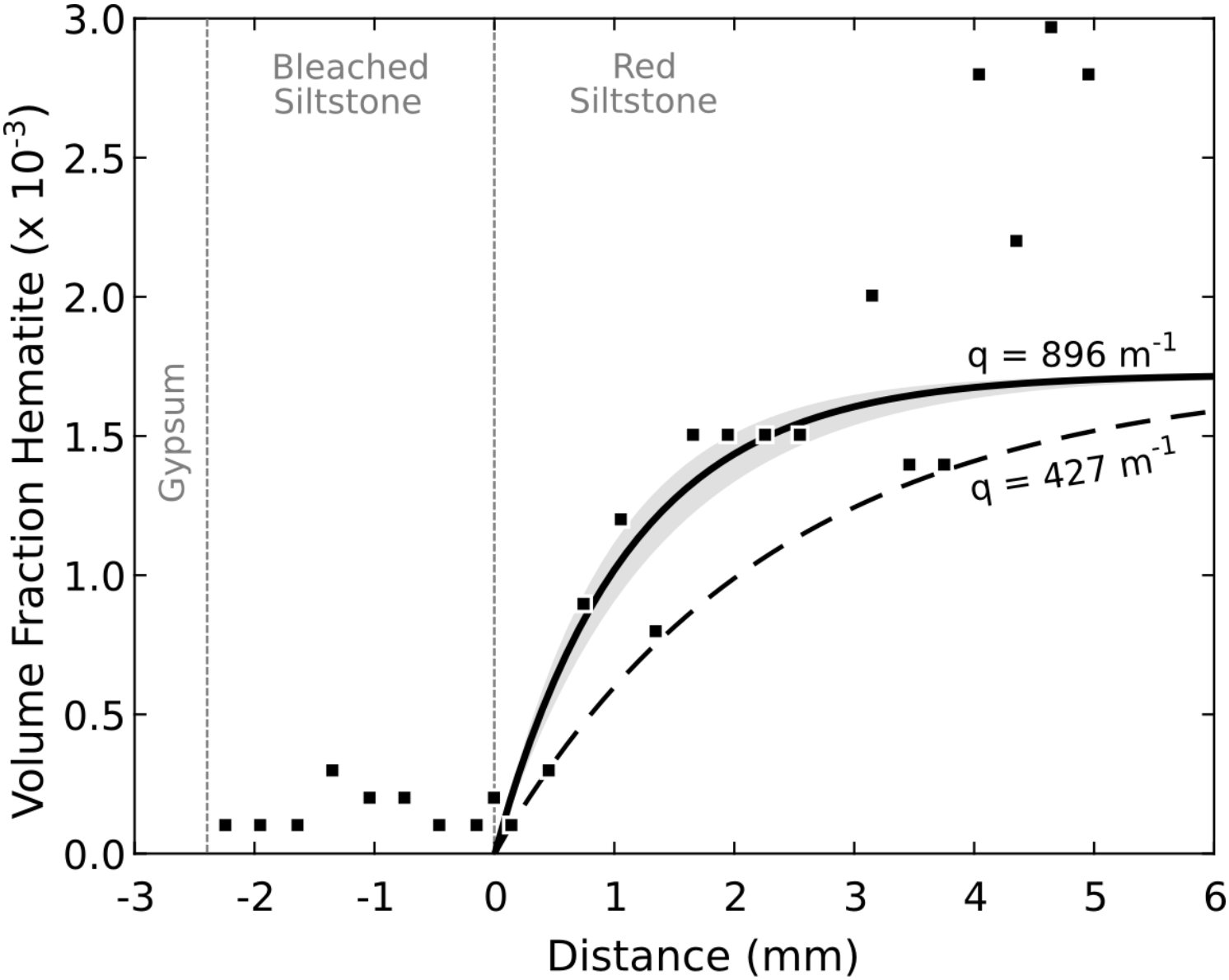
Bleached
Siltstone
Red
Siltstone
Gypsum
q = 896 m-1
q = 427 m-1
Volume Fraction Hematite (x 10-3)
Distance (mm)
3.0
2.5
2.0
1.5
1.0
0.5
0.0
-3
-2
-1
0
1
2
3
4
5
6

Figure 6

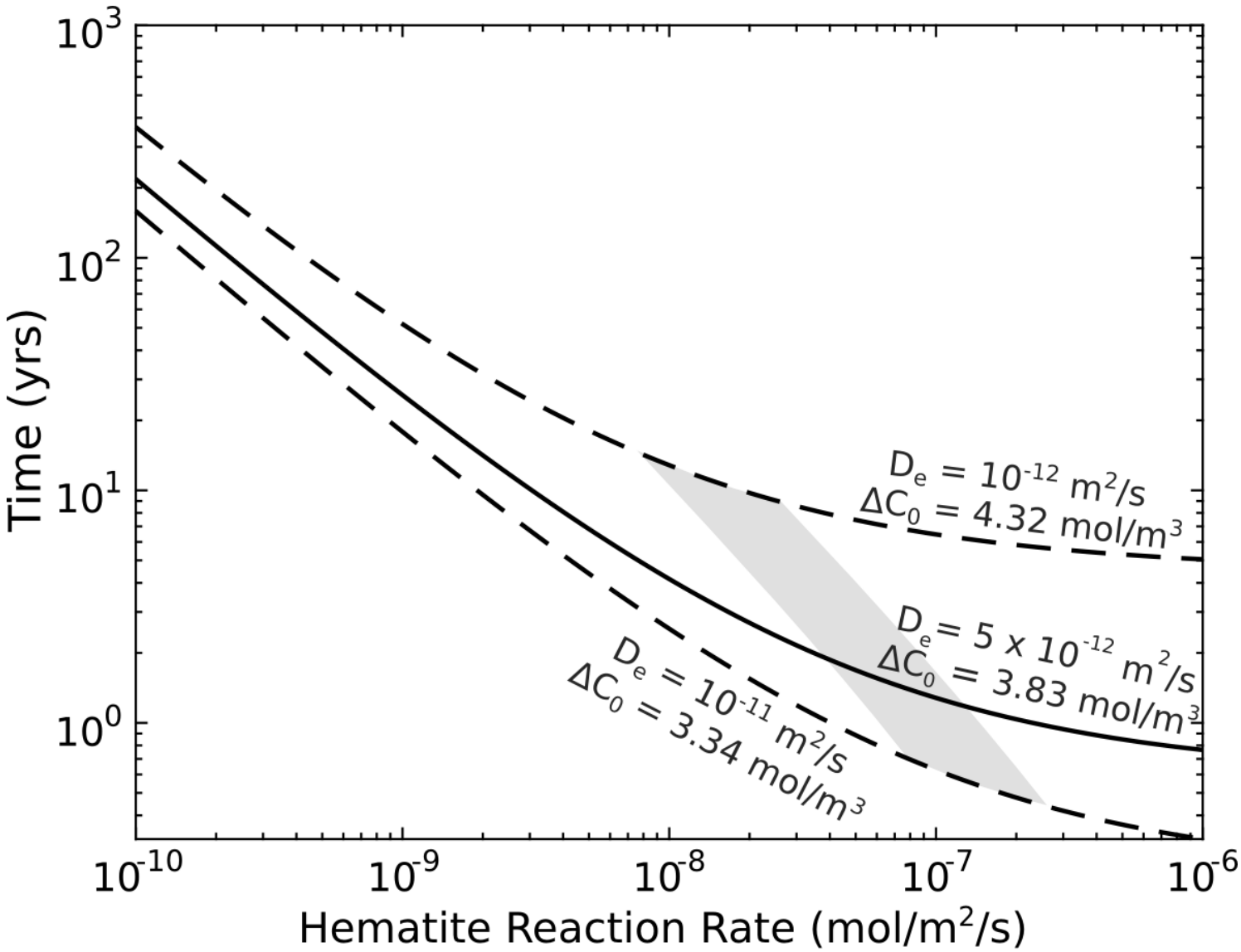
Time (yrs)
Hematite Reaction Rate (mol/m²/s)
10^3
10^2
10^1
10^0
10^{-10}
10^{-9}
10^{-8}
10^{-7}
10^{-6}
$D_e = 10^{-12}$ m²/s
$\Delta C_0 = 4.32$ mol/m³
$D_e = 5 \times 10^{-12}$ m²/s
$\Delta C_0 = 3.83$ mol/m³
$D_e = 10^{-11}$ m²/s
$\Delta C_0 = 3.34$ mol/m³

Figure 7

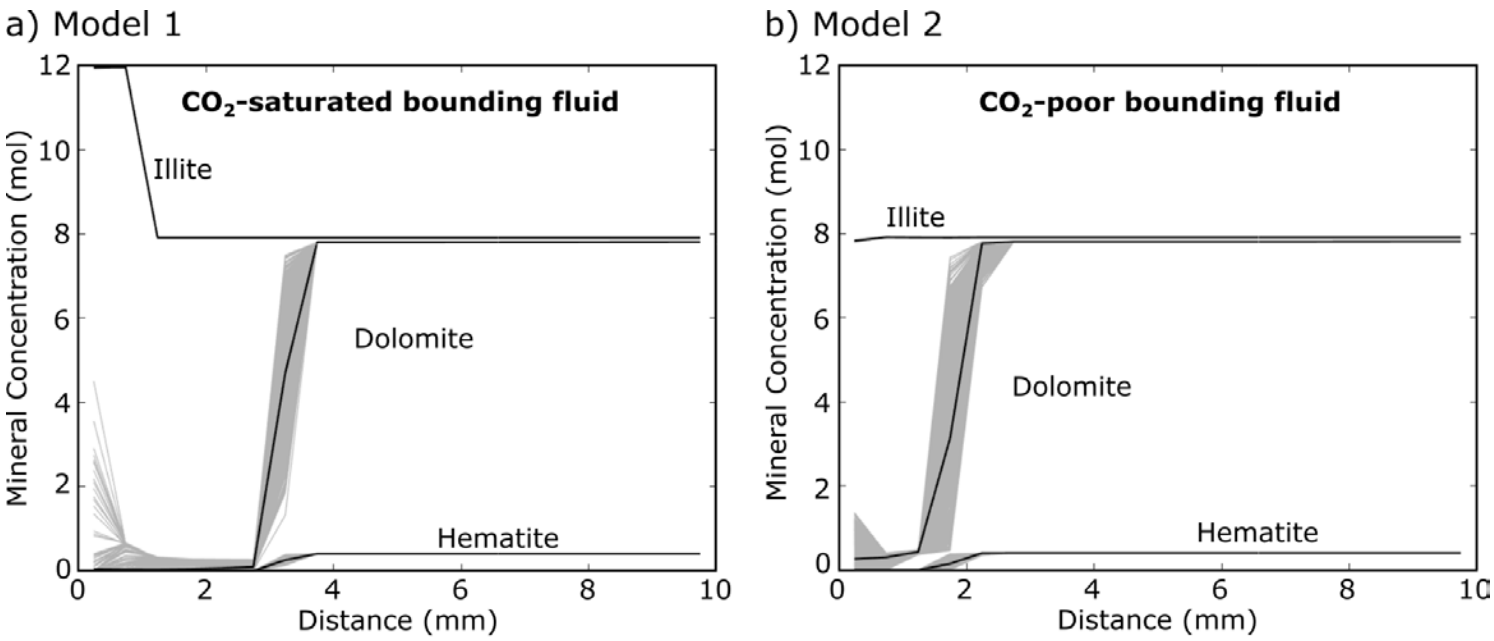
a) Model 1
CO_2-saturated bounding fluid
Illite
Dolomite
Hematite
Mineral Concentration (mol)
Distance (mm)
b) Model 2
CO_2-poor bounding fluid
Illite
Dolomite
Hematite
Mineral Concentration (mol)
Distance (mm)

Figure 8

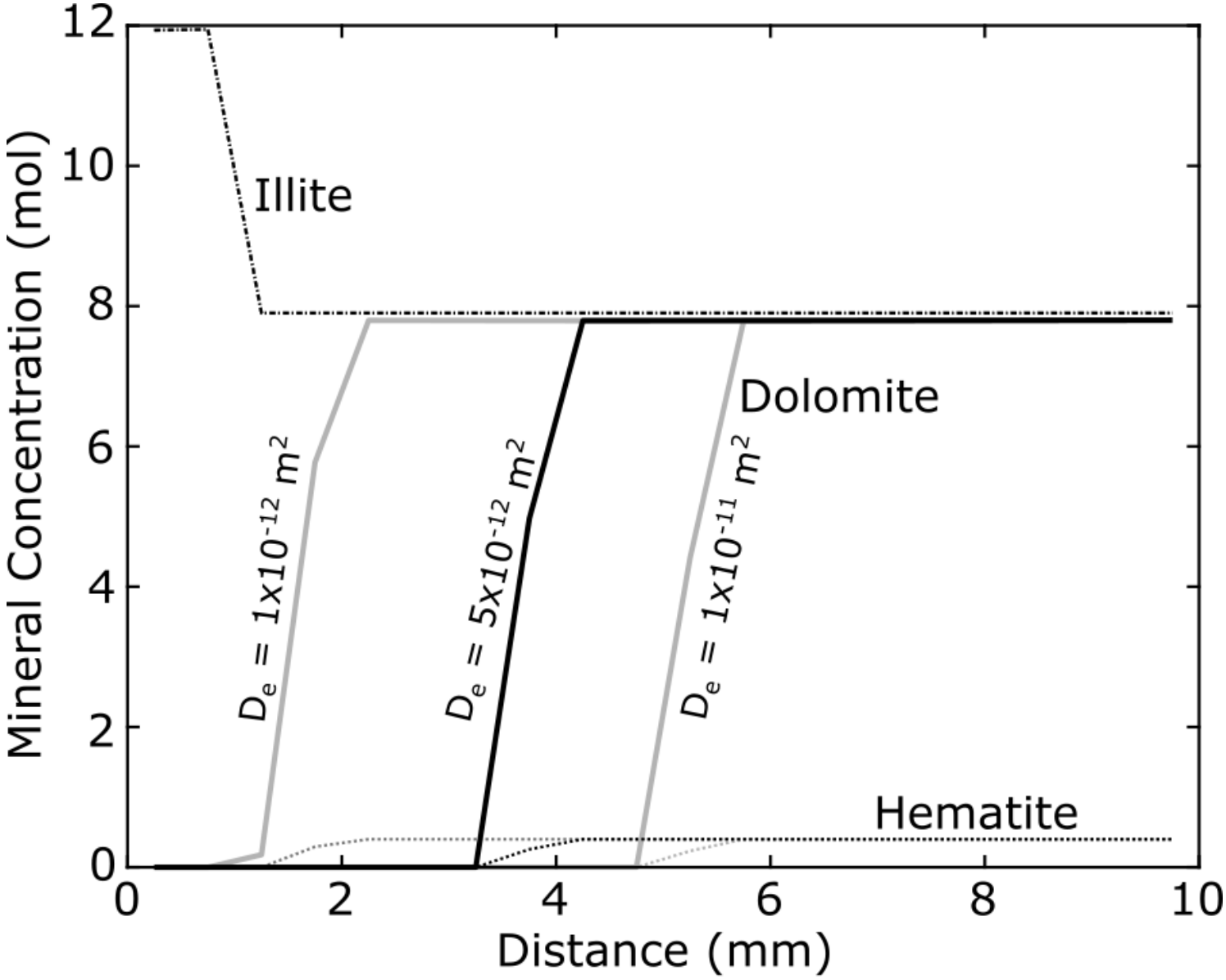
Mineral Concentration (mol)
Distance (mm)
Illite
Dolomite
Hematite
$D_e = 1x10^{-12}\ m^2$
$D_e = 5x10^{-12}\ m^2$
$D_e = 1x10^{-11}\ m^2$
0
2
4
6
8
10
12

Figure 9

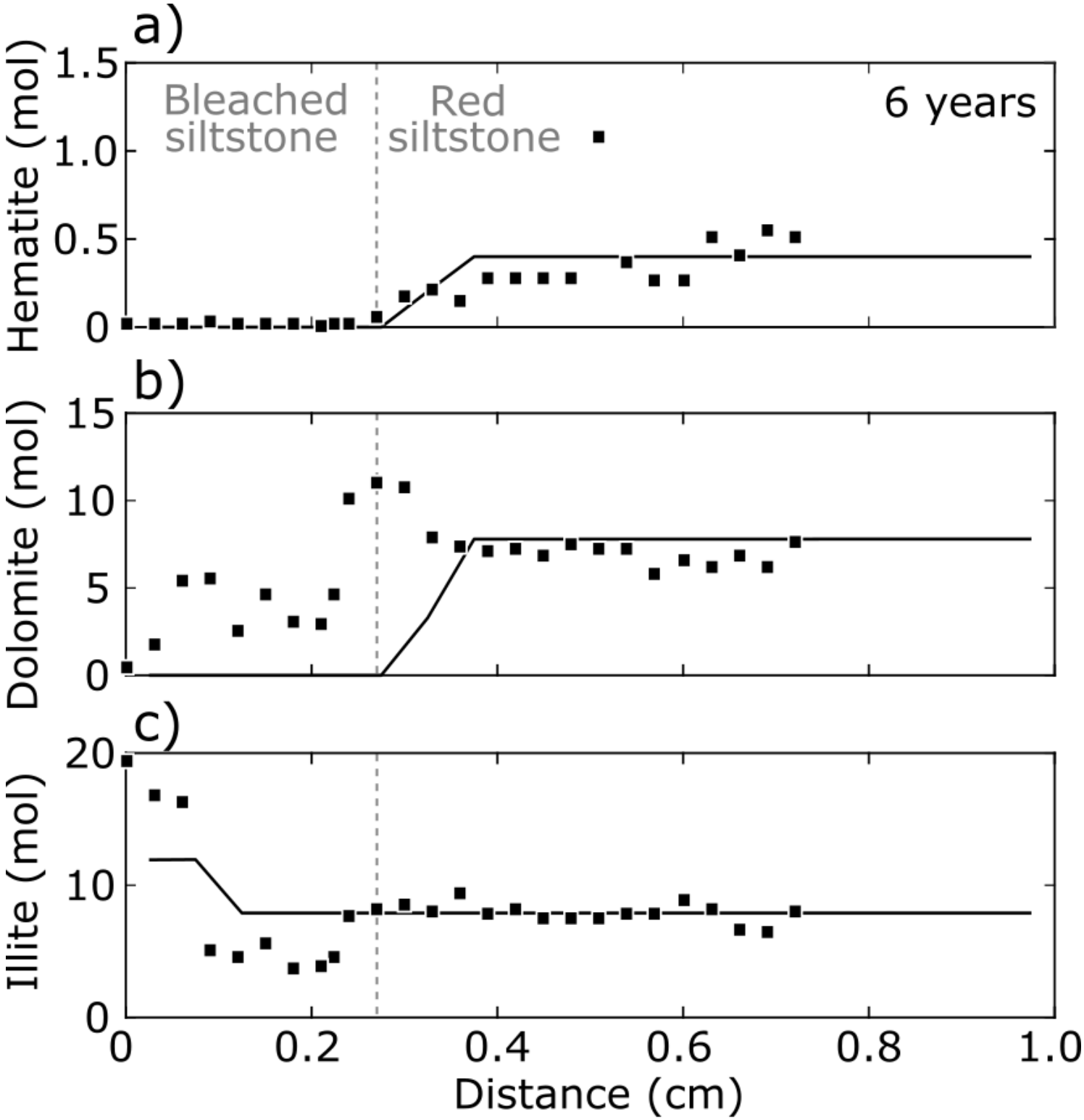
a)
Hematite (mol)
1.5
1.0
0.5
0
Bleached siltstone
Red siltstone
6 years
b)
Dolomite (mol)
15
10
5
0
c)
Illite (mol)
20
10
0
0
0.2
0.4
0.6
0.8
1.0
Distance (cm)

Figure 10